Microwave Radiative Transfer through Clouds Composed of Realistically Shaped Ice Crystals. Part I: Single Scattering Properties

K. FRANKLIN EVANS

Program in Atmospheric and Oceanic Sciences, University of Colorado, Boulder, Colorado

GRAEME L. STEPHENS

Department of Atmospheric Science, Colorado State University, Fort Collins, Colorado

(Manuscript received 27 May 1994, in final form 29 November 1994)

ABSTRACT

This paper presents the results of a detailed study of the microwave single scattering properties of ice crystals expected in cirrus clouds. The discrete dipole approximation is used to compute scattering quantities of particles ranging in size from 30 to 2000 μm at 85.5, 157, 220, and 340 GHz. Five shapes were simulated: solid and hollow columns, hexagonal plates, planar bullet rosettes, and equivalent-volume spheres. The scattering properties were computed for 18 Gamma size distributions with a range of characteristic particle size and distribution width.

The results indicate that particle shape has a significant effect; for example, there is a range of about 3 in extinction over the five shapes for the same size distribution and ice water content. Crystal shape is the dominant effect on the polarization of the scattering, with the thinner shapes having the more polarizing effect. The characteristic particle size has the greatest impact on the extinction and single-scattering albedo, while the distribution width has only a minor effect.

1. Introduction

Remote sensing of clouds using passive measurements of microwave emission has blossomed over the past decade. This interest has been stimulated, in part, by our desire to remotely sense precipitation from space (Simpson et al. 1988) and by the capabilities of the Defense Meteorological Satellite Program (DMSP) in providing the research community with passive measurements at 19, 22, 37, and 85 GHz from the Special Sensor Microwave/Imager (SSM/I) (Hollinger et al. 1990). A significant body of research has recently reported on a number of methods for deriving properties of water vapor, liquid water clouds, and rainfall from these observations (e.g., Alishouse et al. 1990; Tjemkes et al. 1991; Liu and Curry 1993; Greenwald et al. 1993; Wilheit and Chang 1991; Kummerow and Giglio 1994; Wilheit et al. 1994).

For many applications, scattering of microwave radiation by ice particles in the atmosphere looms as an important issue. Microwave remote sensing of precipitation over land relies on relating brightness temperature depressions due to scattering by ice hydrometeors to the rainfall below. Large scattering signatures due to precipitating ice particles have been observed from satellites at frequencies as low as 37 GHz (e.g., Spencer et al. 1983). With the 85-GHz frequency on the SSM/I, Spencer et al. (1989) observed small (up to 10 K) polarization differences near convective cores over land and proposed that they were due to oriented ice particles in stratiform precipitation regions. The effect of ice particles in clouds is also an issue when using the higher frequencies to measure cloud liquid water path. Due to their widespread nature, cirrus clouds may be a source of contamination for microwave temperature profiling at 118 GHz (as discussed by Weinman 1988) and water vapor profiling at 183 GHz.

Microwave radiometers, either newly deployed or currently under development, have frequencies for which scattering by atmospheric ice particles is an important issue. The DMSP SSM/T-2 and National Oceanic and Atmospheric Administration Advanced Microwave Sounding Unit (AMSU/B) satellite instruments are designed for water vapor profiling with the 183-GHz line. The National Aeronautic and Space Administration (NASA) is developing a research aircraft–based Millimeter-Wave Imaging Radiometer (MIR) (Gasiewski 1992), which has channels at 89, 150, 183 $\pm$ 1, 3, 7, 220, and 325 $\pm$ 1, 3, 9 GHz. As we will show below, these higher frequencies have a much greater sensitivity to low concentrations and small sizes

Corresponding author address: Dr. K. Franklin Evans, Program in Atmospheric and Oceanic Sciences, University of Colorado, Campus Box 311, Boulder CO 80309.

of ice particles than do previous radiometers, and so a much larger range of ice clouds can be sensed.

There has been a limited amount of work concerning high-frequency passive microwave remote sensing of ice clouds. Wu (1987) used the Advanced Microwave Moisture Sounder with channels at 92 and 183 ± 2, 5, 9 GHz combined with infrared radiometry data to infer the ice water content and geometrical thickness of deep convective clouds. Gasiewski (1992) performed a theoretical study of the use of microwave frequencies from 90 to 410 GHz. Through radiative transfer simulations he examined the sensitivity of the brightness temperatures to water vapor, precipitation, water clouds, and ice clouds. Ice spheres with one-parameter size distributions (tying the average particle size to the mass content) were used, so the issues of ice particle shape and size were not generally addressed. Muller et al. (1994) did a similar theoretical study at AMSU frequencies in which a single-size distribution of ice spheres was used.

Despite the broad relevance of ice particle scattering to microwave remote sensing, a detailed study of the effects of ice crystal shape on both particle single scattering and radiative transfer has yet to be carried out. It is the purpose of this paper to provide a theoretical assessment of the effects of ice crystal microphysics, including properties of size and shape, on microwave transfer at selected frequencies. This study focuses on the microwave single scattering properties of cirrus clouds and so considers horizontally oriented pristine ice crystals. In the following paper (Part II, Evans and Stephens 1995) we explore with theoretical modeling the feasibility of, and possible methods for, high-frequency microwave sensing of the ice water path of cirrus clouds from high-altitude aircraft and satellite.

In the following section of this paper, the discrete dipole approximation (DDA) is introduced as a method for deriving the single scattering properties of ice crystals of complex shape. Tests of the DDA approach are presented in section 3, and scattering results for four frequencies (85.5, 157, 220 and 340 GHz) are presented in section 4 for five different ice crystal shapes. These results are conveniently expressed in the form of functional fits that can be used directly in a first-order scattering radiative transfer model of the microwave brightness temperature depression. The results of this study and the implications for microwave radiative transfer are summarized in the final section of the paper.

2. The discrete dipole approximation

The first step in computing the transfer of microwave radiation through cirrus particles is to model the electromagnetic scattering properties of ice crystals at these wavelengths. Scattering from ice particles in the atmosphere is commonly expressed in terms of Lorenz–Mie theory, in which case the ice crystals are either assumed to be spherical or their scattering properties are assumed to be approximated adequately by spheres. In general, this is a poor approximation because certain basic scattering properties of ice crystals are incorrectly represented; for example, there is little difference between horizontally and vertically polarized radiation.

In this study, the electromagnetic scattering computations are accomplished using the DDA that was first described by Purcell and Pennypacker (1973). For a recent review of the method see Draine and Flatau (1994). The basic concept behind the DDA is to divide the particle into a number of subunits whose size is small compared to the incident wavelength of radiation. These small subunits behave as dipoles in terms of their response to an applied electromagnetic field. Each dipole responds to a sum of the incident plane wave and the fields from all the other dipoles and in turn generates a field that affects the other dipoles. The DDA is also called the coupled dipole method because of this mutual interaction between the subunits. The main computational task of the DDA is to invert the coupled system of dipole interactions for the polarization of each dipole, given a particular incident plane wave. The dipole fields are then combined to compute the resulting far-field scattering amplitudes from which the desired scattering properties may be derived. The DDA is general in that it applies to any particle shape, although computer limitations have restricted the method to particles that are only slightly larger than the wavelength (Goodman et al. 1991). Examples of studies that use the DDA are Singham and Bohren (1987), Draine (1988), O'Brien and Goedecke (1988), Dungey and Bohren (1993), and Flatau et al. (1993). Electromagnetic scattering methods equivalent to the DDA are used extensively in engineering (e.g., Sarkar et al. 1985).

a. DDA theory

The method adopted here follows closely a paper by Goedecke and O'Brien (1988). Starting from Maxwell's equations, it can be shown that the solution for the electric field $\mathbf{E}(\mathbf{r})$ everywhere in space, resulting from the scattering of an incident field $\mathbf{E}^{\text{in}}(r)$ from a dielectric particle, may be expressed as an integral over the particle volume of the Green's function G multiplied by the dielectric polarization $p(r)$. The solution is

$$\mathbf{E}(\mathbf{r})[1 + 4\pi\chi(\mathbf{r})/3] = E^{\text{in}}(r) + \int d^3r' G(\mathbf{r} - \mathbf{r}') \cdot p(\mathbf{r}'). \quad (1)$$

The polarization at points inside the particle is related to the field by $\mathbf{p}(r) = \chi\mathbf{E}(r)$, where χ is the susceptibility, $\chi = (1/4\pi)(m^2 - 1)$, and m is the complex index of refraction. The Green's function is the field

due to a single, harmonically oscillating dipole and depends only on the position relative to the dipole ($\mathbf{R}$):

$$G_{ij}(\mathbf{R}) = \frac{1}{R}\exp(-ikR)\left[k^2(\delta_{ij} - \hat{R}_i\hat{R}_j) - (\delta_{ij} - 3\hat{R}_i\hat{R}_j)\left(\frac{1}{R^2} + \frac{ik}{R}\right)\right], \quad (2)$$

where the subscripts i and j refer to the Cartesian components of the fields and the direction vector $\hat{R}$, and $k = 2\pi/\lambda$ is the wavenumber for the free-space wavelength λ.

Dividing the particle into dipoles is equivalent to discretizing both the field and the Green's function over the volume of the particle. In the current model the particle is divided into cubes of size d, and a discrete form of (1) is used:

$$E_{si}^{\text{in}} = [\chi_s^{-1} + (4\pi/3)(1 - \Gamma)]p_{si} - d^3 \sum_{t \neq s} \sum_j G_{ij}(r_s - r_t)p_{tj}, \quad (3)$$

where s and t are dipole indices. The small but nonzero volume of a dipole contributes to the integral in (1), giving rise to a "self-term" Γ modeled by Goedecke and O'Brien (1988) as

$$\Gamma^{\text{GO}} = \left(\frac{3}{4\pi}\right)^{2/3}(kd)^2 - \frac{1}{2\pi}i(kd)^3.$$

The small imaginary part of Γ is necessary to satisfy the optical theorem relating the total-scattering cross section to the imaginary part of the forward-scattering amplitude. This form of notation for the DDA is entirely equivalent to that involving the dipole polarizability α and dipole moment $\mathbf{P}$, where $\mathbf{P} = \alpha\mathbf{E}$ (e.g., Draine 1988). Purcell and Pennypacker (1973) used the Clausius–Mossotti polarizability

$$\alpha^{\text{CM}} = \frac{3d^3}{4\pi}\frac{m^2 - 1}{m^2 + 2},$$

which is equivalent to $\Gamma^{\text{CM}} = 0$. Draine and Goodman (1993) derived an improved form for the polarizability called the lattice dispersion relation (LDR) by requiring the same dispersion relation for an infinite lattice as for the continuum. In general the LDR depends on the incident direction, but the isotropic form is equivalent to

$$\Gamma^{\text{ILDR}} = \frac{3}{4\pi}(1.8915 + 0.18915m^2)(kd)^2 - \frac{1}{2\pi}i(kd)^3.$$

Draine and Goodman (1993) showed that the LDR is somewhat more accurate for $|m|kd \geq 1/2$ than the self-interaction term used by Goedecke and O'Brien (1988) and in this paper.

Equation (3) defines a coupled linear system that may be solved for the dipole polarizations p_s for a given incident field $\mathbf{E}^{\text{in}}$. The incident plane wave field with direction $\hat{k}'$ is evaluated at the sth dipole according to

$$\mathbf{E}_s^{\text{in}}(\hat{k}') = \mathbf{E}_0\exp(-ik\hat{k}'\cdot r_s),$$

where E_0 represents either the vertically or horizontally polarized field, which we set with a unit amplitude $|E_0| = 1$.

The coordinate system for the electric field polarization is defined by the propagation direction $\hat{k}$ and the vertical z axis. The vertical unit vector $\hat{V}$ is perpendicular to the propagation direction, in the meridional plane, and has a positive z component. The horizontal unit vector $\hat{H}$ is perpendicular to the plane such that $\hat{V} \times \hat{H} = \hat{k}$.

The scattered electric field far from the particle is an outgoing spherical wave with components given by the scattering amplitude matrix multiplied by the incident field vector. In terms of V and H components this is expressed by

$$\begin{pmatrix} E_{vs} \\ E_{hs} \end{pmatrix} = \frac{\exp(-ikr)}{ikr}\begin{pmatrix} F_{vv} & F_{vh} \\ F_{hv} & F_{hh} \end{pmatrix}\begin{pmatrix} E_{vi} \\ E_{hi} \end{pmatrix},$$

which can be taken as the definition of the scattering amplitudes F. The scattering amplitudes represent a linear transformation of the incident electric field vector with propagation direction $\hat{k}'$ into the scattered electric field with direction $\hat{k}$. The scattering amplitudes are easily found from the dipole polarizations using (1) and (2) with $R \to \infty$, giving

$$F_i(\hat{k}) = \sum_j (\delta_{ij} - \hat{k}_i\hat{k}_j)i(kd)^3 \sum_s \exp(ik\hat{k}\cdot\mathbf{r}_s)p_{sj}.$$

This form explicitly shows that the scattering amplitude vector is perpendicular to the propagation direction as required. The Cartesian components F_i are projected onto the polarization directions $\hat{V}$ and $\hat{H}$ for each of the two incident polarizations to generate the four scattering amplitudes (F_{vv}, F_{vh}, F_{hv}, F_{hh}). The set of scattering amplitudes for all incident and outgoing directions contain the complete information about the far-field aspects of the scattering process.

b. Scattering functions and cross sections

The radiative transfer calculations require that the radiation field and scattering properties be expressed in terms of intensity rather than amplitude, and for this the standard Stokes parameters (I, Q, U, V) are used. The scattering process is then expressed with 4×4 Stokes parameter scattering and extinction matrices. While the DDA model computes the scattering properties for all four Stokes parameters, there is a simplification that is used for the modeling in this work. In a thermally emitting atmosphere with a plane parallel geometry and no preferred azimuthal orientation of particles, the radiation field is azi-

muthally symmetric and the U and V Stokes parameters are zero. For application to ice clouds and microwave radiation, the largest source of azimuthal asymmetry would be from the incident radiation (e.g., from subcloud spatial inhomogeneities), and this should in general be small. The two Stokes parameters of interest are thus $I = |E_v|^2 + |E_h|^2$ and $Q = |E_v|^2 - |E_h|^2$.

For an azimuthally symmetric system the relevant scattering properties can be expressed with 2×2 matrices. The scattering matrix is computed from the scattering amplitudes according to

$$M = \frac{1}{2k^2} \sum_l n_l \begin{pmatrix} |F_{vv}|^2 + |F_{vh}|^2 + |F_{hv}|^2 + |F_{hh}|^2 & |F_{vv}|^2 - |F_{vh}|^2 + |F_{hv}|^2 - |F_{hh}|^2 \\ |F_{vv}|^2 + |F_{vh}|^2 - |F_{hv}|^2 - |F_{hh}|^2 & |F_{vv}|^2 - |F_{vh}|^2 - |F_{hv}|^2 + |F_{hh}|^2 \end{pmatrix},$$

where n_l is the number concentration of particles and Σ_l indicates the incoherent sum over an ensemble of particles. Similarly, the extinction matrix is defined in terms of the forward scattering amplitudes according to the fundamental extinction formula as

$$K = \frac{2\pi}{k^2} \sum_l n_l \begin{bmatrix} \mathrm{Re}(F_{vv} + F_{hh}) & \mathrm{Re}(F_{vv} - F_{hh}) \\ \mathrm{Re}(F_{vv} - F_{hh}) & \mathrm{Re}(F_{vv} + F_{hh}) \end{bmatrix}.$$

The scattering matrix is defined for each combination of incident and outgoing directions, and the extinction matrix is defined for each incident direction. Both types of matrices have units of inverse length. The full 4×4 Stokes parameter representation for the scattering and extinction matrices was given in Evans and Vivekanandan (1990) but with scattering amplitudes f defined so that $F = ikf$.

A simpler, though entirely equivalent, basis for the polarization state of the radiation field is $I_V = |E_v|^2$ and $I_H = |E_h|^2$. In this basis the scattering and extinction matrices are

$$M = \frac{1}{k^2} \sum_l n_l \begin{pmatrix} |F_{vv}|^2 & |F_{vh}|^2 \\ |F_{hv}|^2 & |F_{hh}|^2 \end{pmatrix},$$

and

$$K = \frac{4\pi}{k^2} \sum_l n_l \begin{pmatrix} \mathrm{Re}(F_{vv}) & 0 \\ 0 & \mathrm{Re}(F_{hh}) \end{pmatrix}.$$

There are two ways to compute absorption by the particle. One is to subtract the integral of the scattering matrix over outgoing directions from the extinction matrix:

$$\sigma_I = K_{II}(\hat{k}') - \int M_{II}(\hat{k}', \hat{k}) d\hat{k},$$

$$\sigma_Q = K_{IQ}(\hat{k}') - \int M_{IQ}(\hat{k}', \hat{k}) d\hat{k}.$$

The second method is to integrate the power dissipated in the particle for each incident polarization:

$$\sigma_{v/h} = -4\pi k \sum_\alpha d^3 |E_s|^2 \, \mathrm{Im}(\chi_s),$$

$$\sigma_I = (\sigma_v + \sigma_h)/2,$$

$$\sigma_Q = (\sigma_v - \sigma_h)/2.$$

Comparison of the absorption–emission coefficient computed by these two methods is a check on whether a sufficient number of angles have been used to define the scattering matrix.

In order to interface with the radiative transfer computations, the scattering matrix, extinction matrix, and emission vector are computed for a set of incident zenith angles given by Gaussian or Lobatto quadrature formulas. If the particle shape is symmetric around the horizontal plane, then only one hemisphere of incident zenith angles is computed and the other half is filled in by symmetry. Since the particles are assumed to have no preferred azimuthal orientation, the scattering properties are averaged over a number of incident azimuthal angles in the appropriate range (typically 0, π). The outgoing azimuthal angles are evenly spaced in (0, 2π). For the convenience of the radiative transfer, computation of the scattering matrix is expressed as a Fourier series in the difference in azimuthal angle between the incident and outgoing directions. Only the lowest Fourier mode is required given the assumption of azimuthal symmetry.

In so far as scattering is concerned, the sets of dipole positions r_s and susceptibilities χ_s completely define the particle. These positions are determined using a uniform rectangular grid of dipoles. The geometrical center of the particle is set at the origin, and the grid location is adjusted in each dimension so that an integral number of dipoles fits across the particle. The shapes of particles are specified with simple geometrical formulas (e.g., for spheres, cylinders, hexagonal plates, rectangular solids, etc.). The portion of the volume of each cube that lies within the geometrical definition of a particle is computed by laying down a subgrid of typically 1000 points per dipole cube. This volume fraction determines whether the cube becomes a dipole making up the particle and it also may be used to adjust the susceptibility of the dipole. The susceptibility of the partially filled dipoles is adjusted using Lorentz–Lorenz mixing rule by

$$\frac{\chi_{\text{eff}}}{4\pi\chi_{\text{eff}} + 3} = V_f \frac{\chi}{4\pi\chi + 3},$$

where χ_{eff} is the reduced susceptibility and V_f is the volume fraction. The susceptibility of dipoles on the edge of a particle that is partially filled is reduced via this mixing rule as a simple way of better resolving the particle shape. Using this approach for edge dipoles dramatically improves the accuracy of the scattering properties for smaller particles.

The size of the dipoles d is governed by the requirement that the electric field be relatively constant in the dipole cell. This means that the phase variation across a dipole must be small, which we state as $|m|kd \ll 1$. Goedecke and O'Brien suggest $|m|kd \leq 1$ for reasonable accuracy, but the appropriate criterion to use depends on which scattering quantities are being computed (e.g., backscattering requires smaller $|m|kd$). It is shown below that $|m|kd \leq 1$ provides adequate accuracy for this study. Another reason to keep the dipoles as small as possible is to better approximate smooth particle shapes by discrete arrays of dipoles.

c. *Solution methods and computational considerations*

Two methods are used to solve the coupled linear system (3) for the dipole polarizations p_s. The first method treats (3) as a $3N \times 3N$ complex matrix equation $\mathbf{Ap} = \mathbf{E}^{\text{in}}$ and solves for the $\mathbf{p}$ vector using matrix inversion. The diagonal part of the matrix $\mathbf{A}$ contains the dipole susceptibilities and the self terms, while the off-diagonal part has the dipole–dipole interaction terms. The inversion solution method first computes the LU decomposition of $\mathbf{A}$ and then rapidly solves for p for each incident direction $\mathbf{E}^{\text{in}}$. The computer storage requirements for the inversion method go as N^2 while the computer time goes as N^3, where N is the number of dipoles that is proportional to the particle volume. Computer memory rather quickly becomes the limiting factor. For example, 600 dipoles requires nearly 26 MB of storage.

The second solution method takes into account that (3) contains a convolution sum that can be carried out efficiently with an FFT. The equation is solved by using the conjugate gradient method to iterate the p vector until the residuals of the equation are suitably small (Evans and Stephens 1993). This FFT method was also used for solving the DDA problem by Goodman et al. (1991). Each convolution involves an FFT of the dipole polarizations, multiplication by the precomputed transform of the Green's function, followed by an inverse FFT. In order to avoid aliasing, the FFTs for the convolutions must be done on a uniform 3D grid of twice the particle extent in each dimension. The main advantage of the FFT method is that the DDA may be solved rapidly for large numbers of dipoles. The number of conjugate gradient iterations is virtually independent of the number of dipoles, ranging from a few tens to a few hundreds of iterations depending on the problem. Since FFTs take order $N \log^2 N$ operations, the running time for the FFT DDA method basically goes as N, the number of dipoles. There is, however, a rather large factor in front of the order N, because of the number of iterations required and because the FFTs must be done on an array at least eight times larger than the number of dipoles in the particle. Nevertheless, the FFT method makes DDA with hundreds of thousands of dipoles feasible. One disadvantage of the FFT method is that each incident direction must go through the lengthy conjugate gradient iteration procedure. For radiative transfer computations, where the DDA system must be solved for many incident directions, direct matrix inversion is superior for particles composed of approximately 1000 dipoles or less.

3. Tests of the DDA calculations

To validate the DDA model and illustrate the accuracy typically achieved, a comparison was carried out for spherical particles using Lorenz–Mie theory and for oblate spheroidal ice particles with a 0.25 axial ratio using the extended boundary condition method (ECBM) (e.g., Barber and Yeh 1975). The scattering comparison was made at 340 GHz ($m = 1.781 - 0.0033i$), which is the highest frequency considered in this study. The computations were run for a range of particle sizes from 0.06 to 2.00 mm (to 1.00 mm for spheres). The dipole sizes used in these calculations were the same as those used below for column-shaped cirrus particles. The DDA computations used just one incident azimuth angle, and the other parameters were similar to those used for the cirrus particle calculations below. The dipole sizes and total number of dipoles for the various test shapes are shown in Table 1.

The comparisons were made for the I and Q components of the Stokes scattering and extinction matrices. For scattering, the rms difference over the incident and outgoing quadrature zenith angles was computed for the azimuthally averaged scattering matrix, while for extinction the rms difference was computed over the incident zenith angles. A fractional rms difference

TABLE 1. Dipole sizes and number used in the DDA/Mie/EBCM test.

Particle size (mm)	Dipole size (mm)	Sphere dipoles	Spheroid dipoles
0.060	0.006	720	248
0.120	0.011	967	303
0.250	0.022	1 064	344
0.500	0.032	2 536	760
1.000	0.0375	11 531	3287
2.000	0.0725	—	3592

was made by dividing the absolute rms difference by the maximum matrix value encountered over all the angles.

Figure 1 shows the fractional rms difference in extinction and scattering as a function of particle size for spheres and oblate spheroids. The graph shows that the discrete dipole approximation can calculate the scattering properties of different shapes with adequate accuracy. The maximum fractional difference in extinction and scattering (not shown) is typically around 3% for spheres and ranges from 3% to 12% for the oblate spheroids. The accuracy of the DDA improves as the particle size increases. The reason for this is that the greater number of dipoles used for the larger particle sizes better approximate the true shape of the test particles. This also explains why the DDA is poorer for oblate spheroids than the spheres, as fewer dipoles are packed across the minor dimension of these particles (only 2.5 across for the small particles).

These tests, at the shortest wavelength considered, indicate that the DDA error due to the approximation of the particle shape is probably larger that the error due to the nonzero size of the dipoles for the scattering computations done herein. There are some reasons to believe that the accuracy implied by these test results is somewhat conservative. The dipole sizes used for the test are optimized for approximating columns and not for the test shapes considered here. Also, the cirrus particle shapes modeled below are relatively more angular than the spheres and spheroids considered in these tests and, hence, will be more faithfully modeled by assemblages of cubical dipoles.

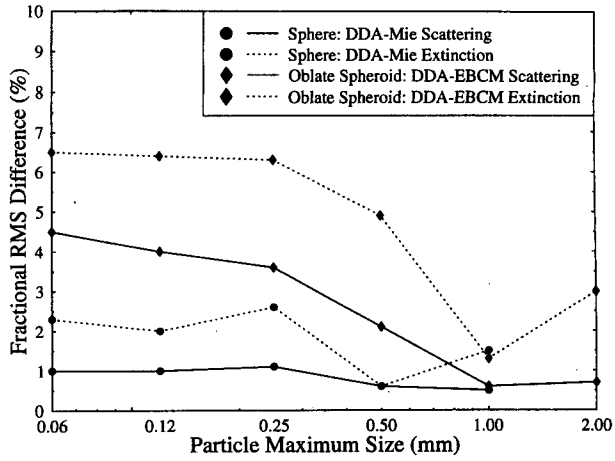

FIG. 1. Fractional rms difference between DDA and Mie/EBCM results for spheres and 0.25 axial ratio oblate spheroids. The rms difference is computed for extinction and scattering matrices at all angles for ice particles at 340 GHz.

4. Ice crystal modeling and single-scattering results

a. DDA modeling

The scattering results are shown for four frequencies (85.5, 157, 220, and 340 GHz). The choice of these frequencies was guided by the channels that exist either on current sensors or by channels proposed for future instruments. The 85.5-GHz channel is on SSM/I, and 157-GHz was a planned channel for AMSU/B. The MIR has channels near all four of these frequencies. Since the microwave scattering properties of ice change relatively slowly with frequency, the results presented below may be considered to correspond to a broader range of frequencies.

For this work, five ice crystal shapes were chosen: solid columns, hollow columns, hexagonal plates, planar rosettes, and spheres. Bullets were not modeled separately, as their shape and aspect ratios are similar to columns. The long axes of the particles were assumed to be randomly oriented in the horizontal plane as a result of aerodynamic forces. Ono (1969) observed that columns and plates fall in this orientation, and lidar studies (e.g., Platt et al. 1978) tend to confirm this. Since columns are expected to rotate about their long axis, solid columns were modeled by cylinders, while hollow columns were modeled by cylinders with cones removed from each end. Modeling by cylinders is justified also because at the wavelengths considered here the detail in the hexagonal columns is not resolved. In nature, rosette crystals are often complex in shape. To simplify matters, a rosette crystal is represented in the scattering calculations by four coplanar cylinders that meet at right angles, which represent one extreme of aspect ratio. Calculations for spheres are also presented for comparative purposes and represent the other extreme of an aspect ratio of unity. To simulate the density of spatial crystals decreasing with size, the spheres are modeled by a smaller equivalent volume of solid ice, with volume depending on size as $V = \pi/6D^3(D/10\ \mu\text{m})^{-1/2}$.

The scattering was computed from 13 discrete maximum particle dimensions from 30 to 2000 μm (intervals of about 1.4), and the scattering was determined by appropriately weighting the properties of each of these 13 single particles by a specified value of a particle concentration as described below. The aspect ratio of the crystals was taken from empirical formulas developed by Heymsfield (1972): namely, $h = 0.260D^{.927}$ for columns, $h = 0.0141D^{.474}$ for plates, $h = 0.1526D^{.7856}D < 300\ \mu$m, and $h = 0.0630D^{.532}D > 300\ \mu$m, for bullets in rosettes, where h is the thickness (centimeters) and D is the maximum particle dimension (centimeters). The maximum particle dimension D is used to characterize the particle size, rather than the equivalent-volume sphere diameter D_{eq}, because the maximum particle extent is usually what is reported in cirrus microphysical measurements. Figure 2 shows the volume versus particle size for the five shapes considered in this study. The ordering of volume

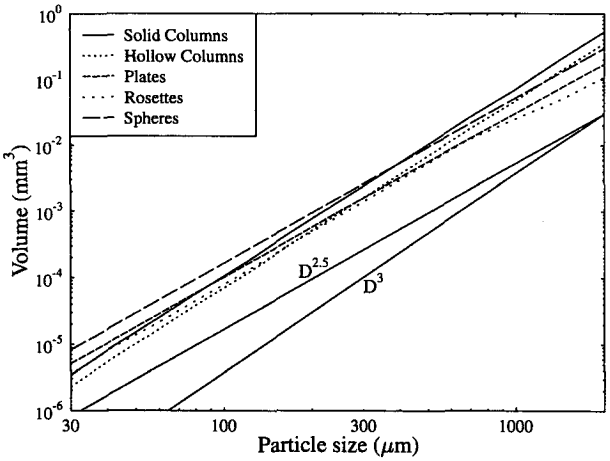

FIG. 2. Particle volume vs size for the five particle shapes. Also plotted for comparison are $D^{2.5}$ and D^3 sloped lines.

with shape varies with the particle size because of the different aspect ratio functions.

The scattering properties for the spheres were computed using Lorenz–Mie theory, while those for the other four shapes were computed using the DDA method. Information about the major and minor dimension, dipole size, number of dipoles, and DDA solution method used to produce these results are listed in Table 2. The dipole size relative to the wavelength ($|m|kd$) was as high as 0.92 for the 2.0-mm column at 340 GHz. A test comparing this case to one with half the dipole size (11 880 dipoles) gave an rms fractional difference of 0.0015 for the scattering matrix and 0.013 for the extinction matrix. The index of refraction for ice at −60°C (Warren 1984) used at the four frequencies (85.5, 157, 220, and 340 GHz) is given in Table 3. The Lorentz–Lorenz mixing rule was used for edge dipoles, and other dipoles were assumed to be solid ice. The scattering properties were computed for eight Lobatto quadrature zenith angles per hemisphere (incident and outgoing). The scattering matrix was averaged over 16 outgoing azimuth angles, and the horizontal orientation averaging was done with 8 incident azimuths over a 180° range. Tests at the highest frequency and largest particle size indicated that the error due to using 8 incident angles for the azimuthal averaging was negligible. The matrix inverse solution method was used when allowed by available memory, as it was substantially faster because of the many incident directions used. The conjugate gradient iterations for the FFT solution method were done until a solution accuracy of 10^{-4} was reached. (The average number of iterations ranged from 14 to 101 per DDA run.)

b. *Discrete size distributions*

The scattering properties (extinction, scattering, and emission) derived for the 13 discrete sizes were weighted according to the Gamma size distributions, defined here by

$$N = aD^{\alpha}e^{-bD} \quad b = \frac{\alpha + 3.67}{D_m},$$

where N is the number concentration per size interval and the distribution is defined by D_m and α; D_m is the median of the distribution of the dimension D to the third power. This is not the median of the volume distribution, because the particle volumes increase more slowly than the third power. The parameter α is related to the width of the distribution by

$$\frac{\langle (D - \langle D \rangle)^2 \rangle}{\langle D \rangle^2} = \frac{1}{1 + \alpha},$$

such that the distribution narrows as α increases. The Gamma distribution has been used by Matrosov et al. (1994) for radar remote sensing of cirrus. Kosarev and Mazin (1989) analyzed many cirrus size distributions and found that Gamma distributions were an adequate representation, with the width parameter α usually ranging from 0 to 2. The Gamma distribution was chosen because the two parameter distributions can simply represent a variety of size distributions.

Because there are only 13 particle sizes, care must be taken when converting the size distribution integral to a weighted sum. In the procedure used here, each discrete size D_i represents a range of sizes from D_i^l to D_i^u. The integral is approximated by

$$\int_0^{\infty} N(D)k(D)dD \approx \sum_{i=1}^{n} k(D_i) \int_{D_i^l}^{D_i^u} N(D)\left(\frac{D}{D_i}\right)^p dD = \sum_{i=1}^{n} N_i k(D_i),$$

where k represents all the scattering quantities being summed together. The $(D/D_i)^p$ factor takes into account that the scattering properties are not constant but generally increase over the size interval. The power p should be the average power-law increase of the scattering properties. For this work we set $p = 3$. (For solid columns at 340 GHz there was only about 1% difference in the resulting scattering properties between $p = 3$ and $p = 4$.) For Gamma distributions, the weights for the sum are

$$N_i = aD_i^{-p} b^{-(\alpha+p+1)}[\Gamma(\alpha + p + 1, bD_i^u) - \Gamma(\alpha + p + 1, bD_i^l)],$$

where Γ is the incomplete Gamma function $\Gamma(a, x) = \int_0^x t^{a-1}e^{-t}dt$. Since the D_i were chosen with logarithmic spacing, the size ranges were set to the geometric mean of the particle sizes; $D_i^l = (D_{i-1}D_i)^{1/2}$ and $D_i^u = (D_iD_{i+1})^{1/2}$. At the end points, we choose $D_1^l = 10$ μm and $D_n^u = 2000$ μm.

Using the above procedure 18 Gamma size distributions for each of the five shapes were constructed.

TABLE 2. Particle sizes and DDA dipole layouts.

DDA setup for columns					
			Total dipoles		
Major dim (μm)	Minor dim (μm)	Dipole size (μm)	Solid columns	Hollow columns	Method
2000	580	72.5	1680	1416	FFT
1400	420	52.5	1620	1356	FFT
1000	300	37.5	1620	1356	FFT
700	220	44.0	400	356	inversion
500	160	32.0	400	356	inversion
350	115	23.0	400	356	inversion
250	85	22.0	192	176	inversion
170	60	15.0	192	176	inversion
120	43	11.0	176	168	inversion
80	30	8.0	160	152	inversion
60	23	6.0	160	152	inversion
40	16	4.0	160	152	inversion
30	12	3.0	160	152	inversion

Setup for plates					Setup for rosettes			
Major dim (μm)	Minor dim (μm)	Dipole size (μm)	Total dipoles	Method	Minor dim (μm)	Dipole size (μm)	Total dipoles	Method
2000	66	66	645	inversion	190	64	720	FFT
1400	56	56	442	inversion	150	50	624	inversion
1000	47	47	326	inversion	130	44	387	inversion
700	40	40	228	inversion	110	37	315	inversion
500	34	34	159	invesion	85	30	279	inversion
350	29	29	115	inversion	64	22	336	inversion
250	25	25	78	inversion	49	17	243	inversion
170	20	20	60	inversion	36	12	243	inversion
120	17	17	48	inversion	27	9	288	inversion
80	14	14	26	inversion	20	7	240	inversion
60	12	12	25	inversion	16	6	192	inversion
40	10	10	16	inversion	12	4	192	inversion
30	9	9	12	inversion	9	3	192	inversion

These were made from six values of D_m (70, 100, 150, 250, 400, 700 μm), which were chosen to cover the observed ranges of sizes (e.g., Heymsfield et al. 1990). For each D_m three values of α (0, 1, 2) were chosen.

The effective radius is often used when relating the microphysical and radiative aspects of clouds. The effective radius, r_{eff}, is defined for spherical particles as the ratio of the third moment of the size distribution to the second moment. An equivalent quantity for nonspherical particles is $\langle V\rangle/\langle A\rangle$, which is the ratio of the particle volume averaged over the size distribution to the average projected particle area. This quantity depends on the particle shape and orientation as well as the size distribution (for spheres $\langle V\rangle/\langle A\rangle = 4r_{\text{eff}}/3$). For solid columns with $\alpha = 1$ and a nadir view $\langle V\rangle/\langle A\rangle = 0.17D_m^{0.92}$ in units of centimeters. Table 4 lists effective size for a nadir view for the five shapes and Gamma size distributions with $\alpha = 1$.

TABLE 3. Index of refraction of ice for the four frequencies.

Frequency (GHz)	Wavelength (cm)	Index of refraction (−60°C)
85.5	0.351	(1.778, −0.0012)
157	0.191	(1.779, −0.0019)
220	0.136	(1.780, −0.0024)
340	0.088	(1.781, −0.0033)

TABLE 4. Nadir effective size for five shapes and six distributions.

	$\langle V\rangle/\langle A\rangle$ (μm)				
D_m (μm)	Column	Hollow	Plate	Rosette	Sphere
70	18.3	12.2	12.1	12.6	16.2
100	24.6	16.4	14.1	16.1	19.0
150	35.4	23.5	17.1	21.9	23.1
250	56.3	37.5	22.0	32.6	29.8
400	86.5	57.7	27.6	46.8	37.7
700	144.4	96.4	35.9	69.2	49.8

There are two areas one could question the accuracy of the discrete distribution in approximating a continuous Gamma distribution—whether the smallest size is small enough, and whether 13 sizes are enough. If the volume of the particles goes as $D^{2.5}$, then the size distribution with the smallest particles ($D_m = 70$ μm, $\alpha = 0$) has 13% of its mass below the smallest discrete size (30 μm), though only 0.6% below 10 μm. Since the smallest particles are nearly purely absorbing, the extinction goes as the volume, and the discrete size summing procedure should adequately take into account the mass below the smallest discrete size. Most of the size distributions have negligible mass below 30 μm, anyway. One way to test the accuracy of the discrete size distribution is to compare the 13 size distributions with one having many more sizes. This can be most conveniently done for the spherical particles, because the scattering properties of spheres can be rapidly computed. An approximately continuous size distribution was made using the same Gamma distribution procedure above but for 399 5-μm intervals from 10 to 2000 μm. Comparisons were made at 85.5 and 340 GHz for all 18 Gamma size distributions. The fractional difference in extinction was always less than 2.4%, and the difference in single scattering albedo was always less than 0.01.

c. *DDA scattering results*

The results of the DDA and Lorenz–Mie scattering computations are presented here in two different ways. The first is in the form of plots of the single-scattering quantities relevant to the radiative transfer calculations presented in Part II. The second is in the form of functional fits to the results, which are described in the next section.

The microwave single scattering results computed by the DDA and by Mie theory are plotted both for discrete sizes and for size distributions. The results are shown for two angles, nadir and about 49°, which is near the SSM/I observation angle and is typical for the maximum angle of scanning instruments. For horizontally oriented particles, an angle away from nadir must be used to observe polarization signatures. The size distribution scattering results are presented as a function of D_m, since this parameter characterizes the particle size distribution.

The extinction is a rough measure of how much the ice crystals will depress the brightness temperature. Figures 3a,b show extinction at nadir as a function of particle size for the five shapes at 85 and 340 GHz, respectively. The normalization is such that are 10 particles per cubic meter if the extinction has units of per kilometer. The extinction increases dramatically with size and, as expected, is largest at the highest frequency. Three regimes can be identified for the rate of increase of extinction with particle size. For small particles (<300 μm at 85 GHz, or <100 μm at 340 GHz)

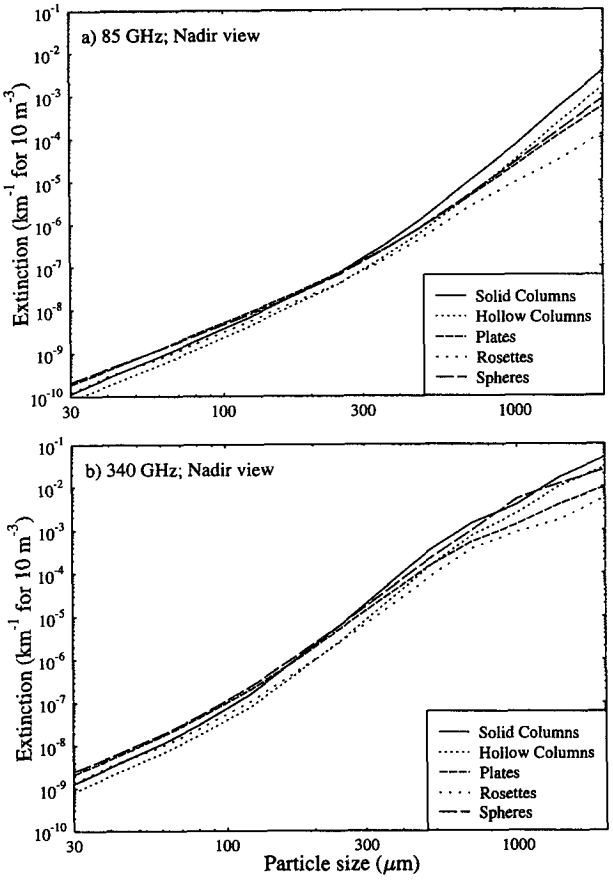

FIG. 3. Extinction vs particle size at (a) 85 and (b) 340 GHz.

absorption dominates, and the extinction is proportional to the particle volume, which is less than the third power of size because of the aspect ratio changing with particle size. For larger particles, scattering dominates, and the extinction goes as the square of the volume, as long as scattering remains in the Rayleigh regime (<500 μm at 340 GHz). Beyond the Rayleigh regime, the extinction curve increases more slowly again with particle size. The difference in extinction between the shapes can primarily be accounted for in terms of the difference in the crystal volumes (see Fig. 2).

Extinction is presented as a function of size distribution parameter D_m for distributions defined by a fixed ice water content of 0.01 g m^{-3}. Figure 4 shows the effect of the size distribution width parameter α on the scattering by columns and spheres at 340 GHz. The width of the distribution is relatively less important than the mean size in determining the scattering properties. The widest distribution generally has the highest extinction due to its greater number of larger particles. There is a similar behavior in other scattering properties (not shown), so that the wider distribution behaves as if it had a slightly larger mean particle size. Because the effect of the distribution width is small, and to sim-

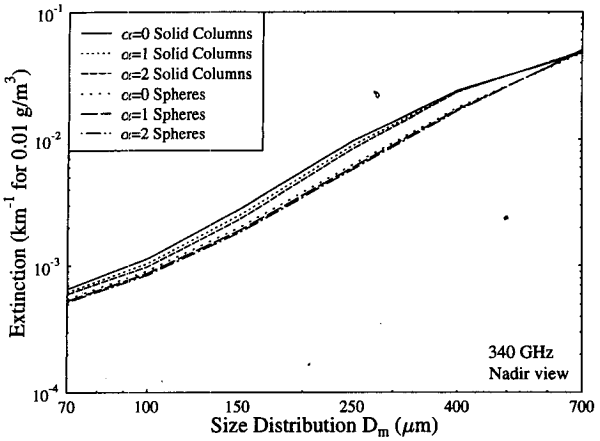

FIG. 4. Extinction vs size distribution for columns and spheres at 340 GHz.

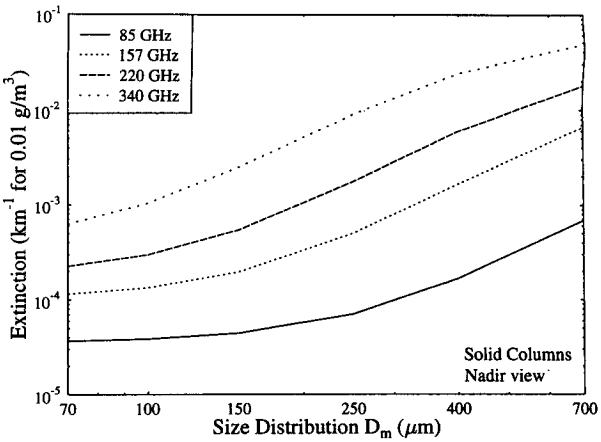

FIG. 6. Extinction vs size distribution for solid columns at four frequencies.

plify the plots, only the $\alpha = 1$ distributions are shown hereafter.

Figure 5 shows the extinction at 220 GHz for all five shapes as a function of D_m. Although all the distributions have the same ice water content (IWC), there is a range up to a factor of 3 in the extinction between the various shapes. Rosettes generally have the smallest extinction, and for distributions defined by larger values of D_m solid columns attenuate the most. The extinction for distributions of solid columns at all four frequencies is shown in Fig. 6. The extinction increases dramatically with frequency. In addition, the way the extinction increases with the distribution D_m varies with frequency. Figure 7 illustrates how the extinction differs at the two observation angles considered (0° and 49°). In general, the nadir angle has higher extinction because radiation at this angle is exposed to the largest cross-sectional area—an effect largest for flat thin plates.

The ratio of extinction for vertical polarization to that for horizontal polarization at 49° is shown in the next two figures. This ratio is a simple way of characterizing how much the ice particles polarize the microwave radiation that upwells through cirrus clouds. Since the horizontal-polarization extinction is larger for horizontally oriented particles, the polarization ratio is less than 1. Spheres are not shown, because their polarization ratio is always 1. Figures 8a,b are plots of the extinction polarization of four shapes as a function of particle size for 85 and 340 GHz, respectively. Plates polarize most, having a ratio of around 0.5 owing to their thinness, followed by rosettes and then columns. Hollow columns are slightly less polarizing than solid columns. There is a tendency for the polarization ratio to decrease with particle size as the aspect ratio decreases (see 85-GHz plot). At 340 GHz there are large oscillations in the polarization ratio with particle size. This is a manifestation of the non-Rayleigh scattering

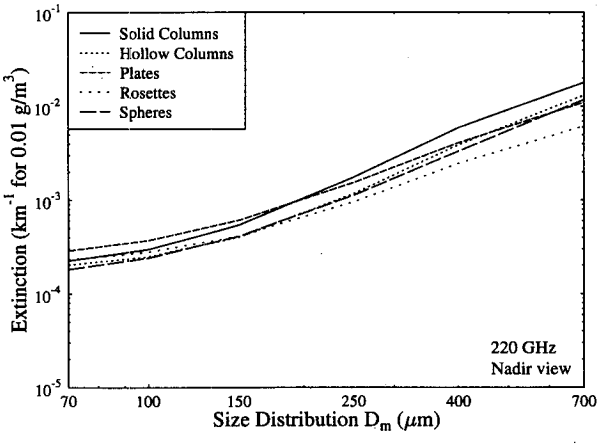

FIG. 5. Extinction vs size distribution for five shapes at 220 GHz.

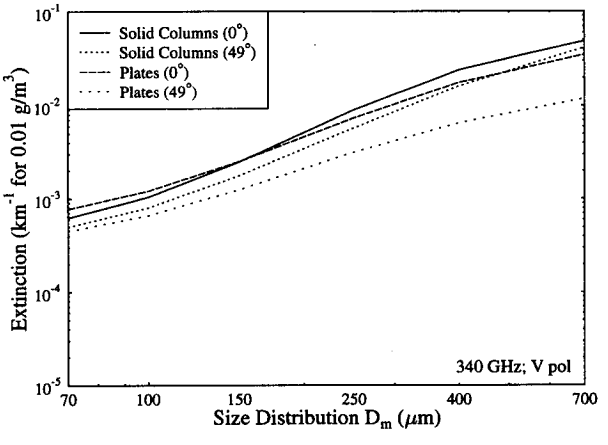

FIG. 7. Extinction vs size distribution for columns and plates at 0° and 49°.

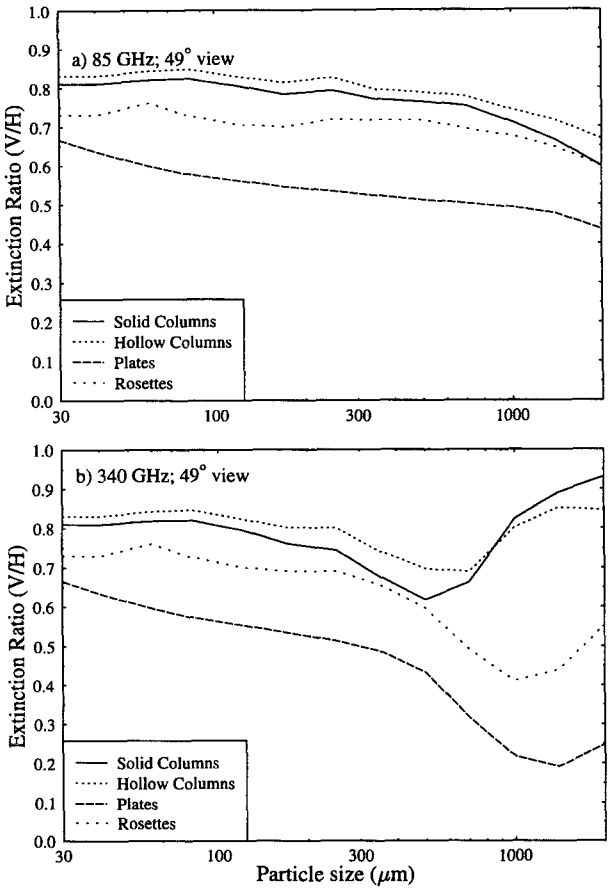

FIG. 8. Extinction polarization ratio vs particle size for four shapes at (a) 85 and (b) 340 GHz.

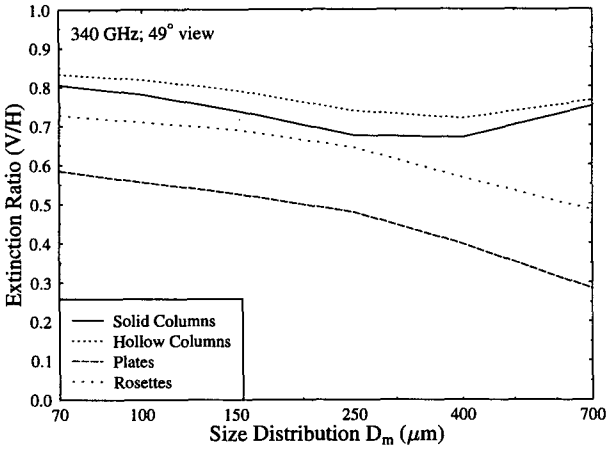

FIG. 9. Extinction polarization ratio vs size distribution for four shapes at 340 GHz.

regime, for which the polarization ratio seems especially sensitive. This non-Rayleigh behavior starts at particle sizes of 300–500 μm at 340 GHz and is apparent at 1000 μm at 157 GHz. One way of explaining the oscillations in the polarization ratio is that the two polarizations see different effective particle sizes due to the nonsphericity of the particles. This means that where the extinction size dependence begins to oscillate—beyond the Rayleigh regime—the two polarizations will be out of phase, so the polarization ratio will oscillate. Averaging over a size distribution, as shown in Fig. 9, reduces the oscillations in the polarization ratio, although these are not eliminated. Thus, the polarization ratio depends on both the particle shape and, to a lesser extent, the size distribution.

The single scattering albedo is crucial for understanding the radiative transfer process of microwave radiation in cirrus. Low albedo means that radiation interacts with the cirrus particles by absorption and emission, whereas high albedo means that radiation interacts primarily through scattering. The single scattering albedo as a function of particle size is shown in Fig. 10 for solid columns at the four frequencies. For all frequencies the smallest particles (D = 30 μm) have an albedo near 0, while the largest particles (>1000 μm) have an albedo near 1. The transition from absorbing to scattering behavior varies considerably with frequency from 330 μm at 85 GHz to 110 μm at 340 GHz for albedo of 0.5. A similar behavior occurs for distributions of particles (Fig. 11). At 85 GHz only the two largest size distributions (with $D_m \geq 400$) have a single scattering albedo above 0.75, while for 340 GHz four size distributions (with $D_m \geq 150$) have albedos above 0.75. Figure 12 shows the single scattering albedo for size distributions for the five particle shapes at 220 GHz. While the variation in albedo with particle shape is not as large as with frequency, there is significant variation, with larger volume shapes (columns) scattering more than smaller volume shapes (rosettes). There is very little change in albedo with polarization or angle.

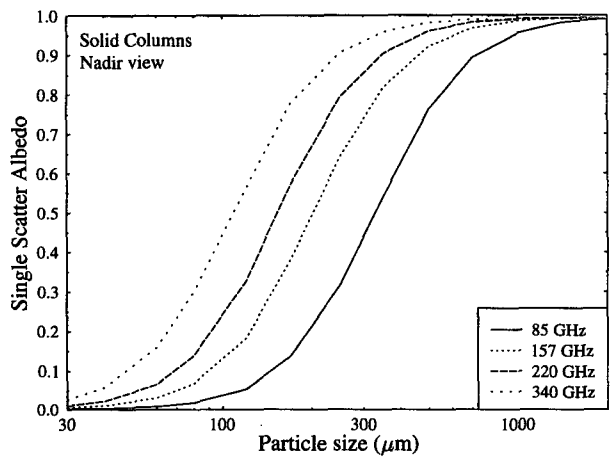

FIG. 10. Single scattering albedo vs particle size for solid columns at four frequencies.

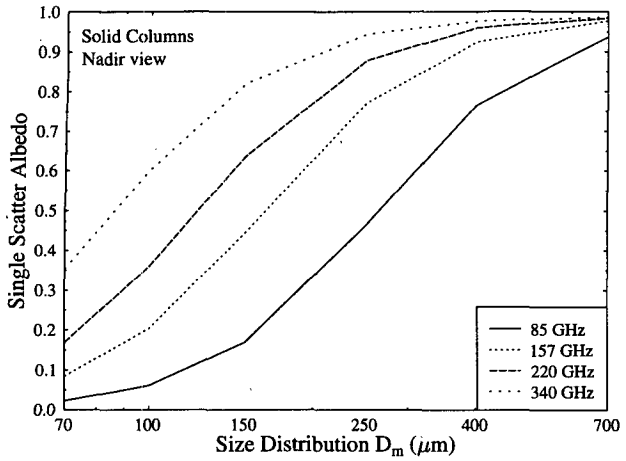

FIG. 11. Single scattering albedo vs size distribution for columns at four frequencies.

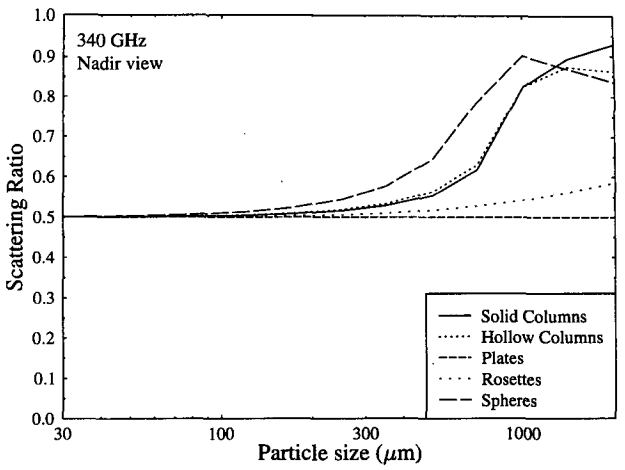

FIG. 13. Scattering ratio vs particle size for five shapes at 340 GHz.

The last single scattering quantity to consider is a measure of the degree of forward scattering. This is important for radiative transfer because more forward scattering to the radiometer will decrease the brightness temperature depression. The usual measure of the amount of forward scattering is the asymmetry parameter, which is the cosine-weighted average of the phase function. That cannot be computed from the azimuthally averaged scattering matrix calculated here, except at nadir incidence. Instead we use a scattering ratio, defined for each upwelling, outgoing angle, as the ratio of the integral of the scattering matrix over upwelling incident angles to the integral over all incident angles. It is the fraction of scattered radiation that would come from upwelling incident angles if the sample was isotropically illuminated by unpolarized radiation. Figure 13 shows the scattering ratio as a function of particle size for the five shapes at 340 GHz. Small particles are in the Rayleigh regime, scattering forward as much as back, so the scattering ratio is 0.5. For spheres and columns, the largest particle sizes have some 80% of the radiation scattered into 0° coming from the upwelling incident angles. The thinner shapes have lower scattering ratios at all sizes. For nadir view the scattering ratio for plates stays at 0.5, because they are modeled as one dipole thick. A similar behavior in the scattering ratio occurs for distributions (not shown), with the ratio increasing with distribution D_m for the thicker particle shapes. Figure 14 shows the scattering ratio as a function of size distribution for hollow columns at the four frequencies. The scattering ratio is significantly larger than 0.5 only for the higher frequencies and for distributions with larger particles. The scattering ratio is lower for off-nadir angles (not shown). It is also larger

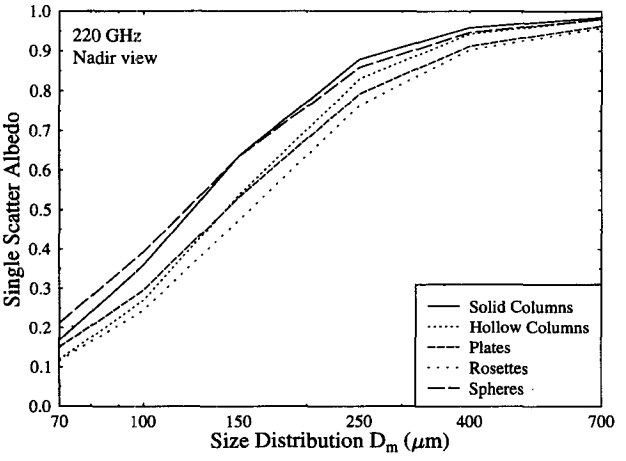

FIG. 12. Single scattering albedo vs size distribution for five shapes at 220 GHz.

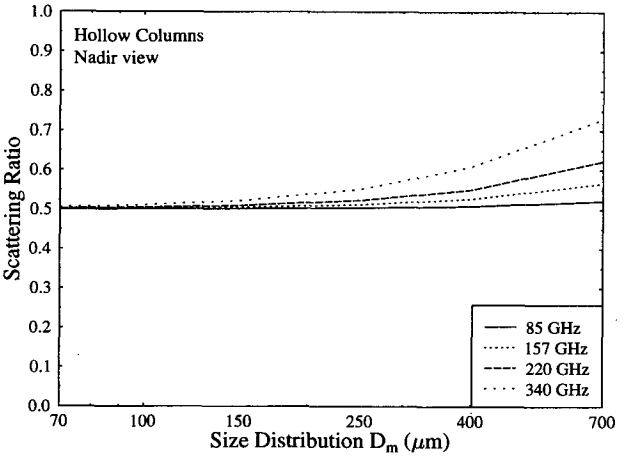

FIG. 14. Scattering ratio vs size distribution for hollow columns at four frequencies.

for vertical than for horizontal polarization for off-nadir angles, even for plates.

d. Fits of scattering results

The scattering results shown above are now presented in the form of tabulated coefficients of functions of particle size. This provides a way for others to use the DDA results for research in microwave remote sensing algorithms without having to go to the complication and expense of generating them. The single-scattering properties are fit to functions for particle sizes ranging from 30 to 2000 μm, thus offering some flexibility for future choices of size distributions. The fits of scattering properties are presented for the four nonspherical particle shapes at 85.5, 157, 220, and 340 GHz for upwelling angles of 0° and 49°. The form of the scattering properties presented here is specifically for use in a simple first-order radiative transfer model.

The scattering properties that are needed for remote sensing at a particular observation angle μ are the polarized extinction $K_p(\mu)$, emission $\sigma_p(\mu)$, and scattering $M_{pp'}(\mu, \mu')$, where p and p' refer to polarization (V or H) and μ' is an incident direction. (In this notation these quantities have units of inverse distance.) It is assumed that the upwelling radiation incident on a cirrus layer is unpolarized. This is partly done to reduce the number of scattering function quantities tabulated but is also justified in terms of actual radiative transfer. Land surfaces are expected to be virtually unpolarized, and a moist atmosphere is optically thick enough at the higher frequencies to totally depolarize the upwelling microwave radiation. Since the upwelling radiation from a clear-sky incident on a cirrus layer is usually a smooth function of zenith angle, its angular structure may be suitably approximated by a quadratic; hence,

$$I(\mu) = I_0 + I_1\mu + I_2\mu^2.$$

Then we need only to consider the first three moments of the scattering function over the upward incident angles:

$$M_p^{(l)}(\mu) = \int_0^1 (M_{p\mathrm{V}}(\mu, \mu') + M_{p\mathrm{H}}(\mu, \mu'))\mu'^l d\mu' \quad l = 0, 1, 2.$$

This reduces the problem to fitting five quantities over particle size (K, σ, $M^{(0)}$, $M^{(1)}$, $M^{(2)}$) for each observation angle/polarization and particle shape.

The optically thin nature of cirrus clouds at microwave frequencies allows the use of a particularly simple formula for the solution to the radiative transfer problem. If the order of scattering solution to the polarized radiative transfer equation is expanded to first order in the layer thickness, the change in upwelling unpolarized radiance as it interacts with the cirrus layer is

$$\Delta I_p(\mu) = \{-K_p(\mu)I(\mu) + \sigma_p(\mu)B(T) + 2\pi[M_p^{(0)}(\mu)I_0 + M_p^{(1)}(\mu)I_1 + M_p^{(2)}(\mu)I_2]\}\frac{\Delta z}{\mu}, \quad (4)$$

where p is the polarization (V or H) and $B(T)$ is the Planck function at the average cloud temperature T.

The assumptions of this first-order radiative transfer model are (i) the cloud is optically thin enough that the order of scattering solution may be expanded to first order in optical depth; (ii) the incident upwelling radiation can be approximated by a quadratic function in μ; (iii) the cloud is above any significant gaseous absorption, so that the incident radiation is the same as the clear-sky top of atmosphere radiance, there is no incident radiation from above the cloud, and extinction and emission properties are due entirely to the cirrus particles; (iv) there is no reflection from the surface or scattering outside the cloud, so the incident radiation is independent of the cloud.

The least-squares fits of the scattering properties as functions of particle size are made to the quantities plotted in the previous section: log of extinction, single-scattering albedo, and three scattering ratios. This was found to be more accurate than fitting directly to the scattering quantities used in (4). The resulting formulas for the fits as function of maximum particle size D are

$$\ln(K) = \sum_{i=0}^{5} K_i(\ln D)^i,$$

$$\omega = 1 - \frac{\sigma}{K} = \frac{1}{1 + (D/\omega_0)^{-\omega_1}} - \omega_2,$$

$$\frac{2\pi M^{(0)}}{K - \sigma} = 0.5 + \exp[M_0^{(0)} + M_1^{(0)}\ln D + M_2^{(0)}(\ln D)^2],$$

$$\frac{M^{(1)}}{M^{(0)}} = M_0^{(1)} + M_1^{(1)}D, \quad \text{and}$$

$$\frac{M^{(2)}}{M^{(0)}} = M_0^{(2)} + M_1^{(2)}D. \quad (5)$$

The scattering ratio $2\pi M^{(0)}/(K - \sigma)$ is the same as plotted in the previous section, because by symmetry of the scattering matrix the integral over all incident directions for a particular outgoing angle is equal to the integral over all outgoing directions for the same incident angle. The constant coefficients in the first and second moment scattering ratios (i.e., $M_0^{(1)}$ and $M_0^{(2)}$) are not fit, because the small-size limit can be used. For nadir angle and horizontal polarization at any angle the $M^{(1)}/M^{(0)}$ ratio is 0.563, while the $M^{(2)}/M^{(0)}$ ratio is 0.400. These ratios (9/16 and 2/5) can be computed theoretically from the Rayleigh phase function, $M(\mu')$

$\propto 1 + \mu'^2$. The two scattering ratios for vertical polarization depend on angle and the Rayleigh limit shape and are listed in Table 5.

The fit coefficients are tabulated for nadir (no polarization) and for $\mu = 0.652$ (49° V and H polarizations) for the four shapes and four frequencies. The coefficients are for extinction K per kilometer for 10 particles per cubic meter and for the particle size D in millimeters. The coefficients for extinction and the resulting rms error in the logarithm over the 13 particles sizes are listed in Table 6. The fit to extinction is, of course, smoother than that computed by DDA, but given the error in the individual DDA calculations, it may be of equivalent or better accuracy. Table 7 contains the fit coefficients for the single scattering albedo and the three scattering ratios. By using the coefficients in these two tables with the formulas in (5), the scattering properties at the available angles for any particle size may be calculated. The scattering quantities, after integration over appropriate size distributions, may be used in (4) to compute the brightness temperature depression from various cirrus crystals at the tabulated microwave frequencies. The accuracy of the scattering fits and the first-order radiative transfer model are explored further in Part II.

TABLE 5. Small size limit of scattering ratios.

Angle/Pol	Shape	$M_0^{(1)}$	$M_0^{(2)}$
0	All	0.563	0.400
H	All	0.563	0.400
49V	Column	0.475	0.305
49V	Hollow	0.473	0.302
49V	Plate	0.496	0.328
49V	Rosette	0.485	0.316

5. Summary and conclusions

The discrete dipole approximation was used to compute microwave single scattering properties of pristine ice crystals appropriate for cirrus clouds. The DDA solves the scattering problem by dividing a particle into many dipolar subunits and finding the dipole polarizations for a given incident wave that satisfy the mutual interaction among the dipoles. Scattering for any particle shape may be computed with the DDA, provided the particle is not more than 3–10 times larger than the wavelength (depending on particle shape and computer resources). An outline of the particular formulation of the DDA used here is given in section 2.

The scattering was computed at four frequencies (85.5, 157, 220, and 340 GHz) that are close to channels on existing or future aircraft and satellite microwave radiometers. Five particle shapes were calculated: solid columns (modeled by cylinders), hollow columns (modeled by cylinders with cones removed), hexagonal plates, bullet rosettes (modeled by four coplanar joined cylinders), and equivalent-volume spheres. The ice crystals are assumed to have their long axis randomly oriented in the horizontal plane by aerodynamic forces. The aspect ratios of the crystals varied with size according to empirical formulas.

The scattering properties were computed for 13 sizes ranging from 30 to 2000 μm. Continuous particle size distributions were simulated by weighting the scattering quantities at the discrete sizes according to the Gamma distribution $N = aD^{\alpha}e^{-(\alpha+3.67)D/D_m)}$ (D is the maximum particle dimension). The parameter D_m is the median of the third power of the dimension and, hence, measures the characteristic particle size, while α is related to the inverse of the width of the distribution. Six values of D_m (70, 100, 150, 250, 400, 700 μm) and three values of α (0, 1, 2) were chosen for a total of 18 Gamma size distributions. The weights used for each particle size were computed with some care to ensure the accuracy of the discrete representation.

The scattering quantities were computed for eight incident and outgoing zenith angles per hemisphere, and two (nadir and 49°) were chosen for further analysis. The single scattering results of the DDA computations are presented in the form of plots and as tabulated fit coefficients. The extinction, single scattering albedo, and the first three moments of the scattering phase function were fit as functions of particle size for each incident angle. The scattering quantities represented by the 14 fit coefficients for each particle shape and incident angle/polarization can be used in a very simple first-order radiative transfer formula to compute the brightness temperature depression.

At the higher frequencies considered here, there are three regimes for extinction as a function of particle size: absorption varying as the particle volume for the smallest particles, Rayleigh scattering varying as the square of the volume, and beyond the Rayleigh regime where the scattering increases more slowly with size. The range in extinction for size distributions with the same IWC is up to a factor of 3 over the five shapes, with rosettes having the least and solid columns the most attenuation. The most important factor for the extinction of a distribution of ice crystals is the characteristic size D_m; for example, at 220 GHz for solid columns the extinction ranges nearly a factor of 80 for the full range of D_m. The range in extinction over the three distribution widths α is only about 20%. The extinction is usually greater for nadir angles, because the particles present the largest cross section to the radiation.

The ratio of extinction for the two polarizations is a measure of the polarizing effect of the nonspherical particles. Plates are the thinnest and most polarizing shape, followed by planar rosettes and then columns. Larger sizes generally have more polarizing effect, but beyond the Rayleigh regime the polarization ratio oscillates with size. The single scattering albedo has a simple behavior with particle size, being near zero for

TABLE 6. Fit coefficients for extinction.

Frequency (GHz)	Angle/Pol	Shape	Error	Extinction coefficients					
				K_0	K_1	K_2	K_3	K_4	K_5
85	0	Column	0.029	−9.5846	5.8211	0.2752	−0.4562	−0.1586	−0.0151
85	0	Hollow	0.026	−10.4004	5.7334	0.3732	−0.4478	−0.1758	−0.0186
85	0	Plate	0.008	−10.7182	4.7919	0.1523	−0.4418	−0.1700	−0.0187
85	0	Rosette	0.072	−11.6516	3.9966	−0.1152	−0.2157	−0.0212	0.0035
85	49H	Column	0.029	−9.6280	5.7582	0.2596	−0.4426	−0.1511	−0.0141
85	49H	Hollow	0.026	−10.4254	5.6903	0.3503	−0.4500	−0.1745	−0.0184
85	49H	Plate	0.009	−10.7955	4.6520	0.0751	−0.4496	−0.1655	−0.0178
85	49H	Rosette	0.072	−11.7066	3.8930	−0.1837	−0.2336	−0.0223	0.0036
85	49V	Column	0.030	−9.9649	5.6017	0.1463	−0.4872	−0.1575	−0.0142
85	49V	Hollow	0.024	−10.7165	5.5820	0.2905	−0.4740	−0.1790	−0.0185
85	49V	Plate	0.007	−11.5026	4.5670	−0.0017	−0.5118	−0.1854	−0.0202
85	49V	Rosette	0.064	−12.0966	3.7607	−0.2670	−0.2177	0.0017	0.0080
157	0	Column	0.025	−7.1243	5.3688	−1.1105	−1.0723	−0.2594	−0.0203
157	0	Hollow	0.028	−7.9582	5.5609	−0.7301	−0.9240	−0.2362	−0.0190
157	0	Plate	0.017	−8.4649	4.4849	−0.7229	−0.6683	−0.1473	−0.0098
157	0	Rosette	0.077	−9.3733	3.8942	−0.7408	−0.2790	0.0546	0.0187
157	49H	Column	0.020	−7.2179	5.4420	−0.6889	−0.6993	−0.1357	−0.0062
157	49H	Hollow	0.025	−8.0258	5.5532	−0.5458	−0.7396	−0.1722	−0.0115
157	49H	Plate	0.029	−8.6615	4.4567	−0.2408	−0.1943	0.0147	0.0088
157	49H	Rosette	0.085	−9.5277	3.7842	−0.5606	−0.0582	0.1344	0.0281
157	49V	Column	0.028	−7.6967	5.2974	−0.3756	−0.3378	−0.0042	0.0096
157	49V	Hollow	0.025	−8.4085	5.4180	−0.3800	−0.5262	−0.0926	−0.0018
157	49V	Plate	0.026	−9.4727	4.0665	−0.6838	−0.4612	−0.0581	0.0013
157	49V	Rosette	0.080	−10.0323	3.4588	−0.7520	−0.0608	0.1603	0.0331
220	0	Column	0.083	−6.2016	4.4136	−1.0397	−0.1403	0.1749	0.0364
220	0	Hollow	0.046	−6.8759	4.8350	−1.0165	−0.4820	0.0144	0.0157
220	0	Plate	0.034	−7.4351	3.8101	−1.0122	−0.3548	0.0322	0.0145
220	0	Rosette	0.078	−8.1965	3.4764	−1.0841	−0.1499	0.1575	0.0335
220	49H	Column	0.027	−6.1145	4.7184	−1.1170	−0.4864	0.0113	0.0142
220	49H	Hollow	0.031	−6.8929	4.9730	−0.8374	−0.4184	0.0187	0.0150
220	49H	Plate	0.028	−7.5005	4.2293	−0.3876	−0.0708	0.0795	0.0165
220	49H	Rosette	0.076	−8.3447	3.5913	−0.6193	0.1943	0.2575	0.0438
220	49V	Column	0.033	−6.5432	4.8466	−0.7449	−0.2974	0.0465	0.0162
220	49V	Hollow	0.026	−7.2658	4.9917	−0.5624	−0.2243	0.0715	0.0201
220	49V	Plate	0.036	−8.5668	3.4933	−0.6732	0.0288	0.1614	0.0288
220	49V	Rosette	0.081	−9.0070	3.1330	−0.6530	0.4069	0.3638	0.0584
340	0	Column	0.090	−5.3261	3.3519	−0.7091	0.7085	0.4753	0.0679
340	0	Hollow	0.071	−5.8476	3.7585	−0.9631	0.2599	0.3201	0.0514
340	0	Plate	0.053	−6.4898	2.8519	−0.7235	0.4645	0.3391	0.0487
340	0	Rosette	0.094	−7.0441	2.6804	−0.8509	0.6552	0.4812	0.0717
340	49H	Column	0.031	−5.1398	3.5197	−1.1359	0.1975	0.2924	0.0466
340	49H	Hollow	0.043	−5.7338	3.9660	−1.1468	−0.0759	0.1828	0.0341
340	49H	Plate	0.032	−6.1160	3.6841	−0.9238	−0.3070	−0.0041	0.0041
340	49H	Rosette	0.050	−6.8820	3.2137	−0.9528	0.1306	0.2373	0.0392
340	49V	Column	0.018	−5.3859	3.9246	−1.0654	−0.0894	0.1427	0.0261
340	49V	Hollow	0.038	−5.9848	4.1881	−1.0964	−0.2565	0.0849	0.0204
304	49V	Plate	0.032	−7.6040	2.8999	−0.3737	0.5438	0.3165	0.0423
340	49V	Rosette	0.038	−7.7266	2.9199	−0.4675	0.6787	0.4291	0.0616

the smallest size and smoothly increasing to near unity for the largest size. The particle size at which the transition happens decreases with frequency, so that the higher frequencies are more strongly scattered. At 340 GHz, distributions of columns with $D_m \geq 250$ μm have single scattering albedos above 0.95. The single scattering albedo is higher for distributions of columns than for rosettes or equivalent-volume spheres because columns have more volume for a given size. The amount of forward scattering increases with particle size and aspect ratio; for example, plates have forward scattering equal to backscattering for nadir view.

Several implications can be drawn for radiative transfer from these single scattering results. For most plausible size distributions of ice crystals at 340 GHz, ice water paths (IWP) of roughly 100 g m^{-2} would be required to have optical depths of order 0.1 and, hence, relatively large brightness temperature depressions. Of course, the extinction and the corresponding ability to detect low concentrations or small ice particles in-

TABLE 7. Fit coefficients for single-scattering albedo and scattering ratios.

Frequency (GHz)	Angle/Pol	Shape	Coefficients							
			ω_0	ω_1	ω_2	$M_0^{(0)}$	$M_1^{(0)}$	$M_2^{(0)}$	$M_1^{(1)}$	$M_1^{(2)}$
85	0	Column	0.3290	3.1206	0.0010	−4.3375	1.8093	−0.0730	0.0154	0.0166
85	0	Hollow	0.3797	3.1777	0.0010	−4.2077	1.8359	−0.0602	0.0121	0.0127
85	0	Plate	0.3923	2.8139	0.0029	−100	0.0000	0.0000	0.0234	0.0257
85	0	Rosette	0.4116	2.8489	0.0093	−6.0093	1.2076	−0.2182	0.0167	0.0183
85	49H	Column	0.3296	3.1056	0.0015	−4.7667	1.7842	−0.1084	0.0090	0.0095
85	49H	Hollow	0.3803	3.1665	0.0013	−4.6385	1.8290	−0.0926	0.0081	0.0083
85	49H	Plate	0.3939	2.7667	0.0052	−100	0.0000	0.0000	0.0140	0.0152
85	49H	Rosette	0.4127	2.8057	0.0114	−33.268	31.890	11.366	0.0115	0.0124
85	49V	Column	0.3297	3.0921	0.0021	−3.4951	1.8776	−0.1043	0.0232	0.0227
85	49V	Hollow	0.3807	3.1549	0.0017	−3.7947	1.8987	−0.0835	0.0185	0.0188
85	49V	Plate	0.3935	2.7693	0.0053	−4.1973	1.7878	0.3905	0.0525	0.0549
85	49V	Rosette	0.4097	2.7876	0.0126	−3.7783	1.8853	0.0147	0.0209	0.0200
157	0	Column	0.2023	2.9868	0.0027	−3.2535	2.2748	0.3749	0.0484	0.0552
157	0	Hollow	0.2339	3.0142	0.0025	−3.0738	2.1102	0.2857	0.0376	0.0415
157	0	Plate	0.2250	2.6560	0.0054	−100	0.0000	0.0000	0.0824	0.0954
157	0	Rosette	0.2428	2.7585	0.0073	−4.8255	1.2362	−0.0186	0.0505	0.0581
157	49H	Column	0.2028	2.9678	0.0033	−3.6658	1.9196	0.2184	0.0029	0.0019
157	49H	Hollow	0.2343	2.9999	0.0029	−3.5028	1.9740	0.1917	0.0105	0.0106
157	49H	Plate	0.2258	2.6021	0.0083	−100	0.0000	0.0000	−0.0002	−0.0010
157	49H	Rosette	0.2433	2.7140	0.0098	−5.2800	1.0247	−0.1497	0.0093	0.0104
157	49V	Column	0.2027	2.9494	0.0043	−2.3426	1.6206	−0.3916	0.0290	0.0262
157	49V	Hollow	0.2344	2.9852	0.0036	−2.6243	1.8034	−0.1367	0.0299	0.0288
157	49V	Plate	0.2246	2.6020	0.0100	−2.8977	1.7969	−0.3306	0.0725	0.0742
157	49V	Rosette	0.2407	2.6887	0.0129	−2.5532	1.6654	−0.4291	0.0362	0.0340
220	0	Column	0.1531	2.9416	0.0038	−2.2802	2.6703	−0.8889	0.0829	0.0970
220	0	Hollow	0.1769	2.9569	0.0037	−2.1774	2.2600	−0.5102	0.0730	0.0832
220	0	Plate	0.1635	2.5939	0.0069	−100	0.0000	0.0000	0.1388	0.1699
220	0	Rosette	0.1794	2.7000	0.0073	−4.1269	1.2862	0.0066	0.0812	0.0975
220	49H	Column	0.1535	2.9199	0.0044	−2.9142	2.0554	0.1267	0.0031	0.0015
220	49H	Hollow	0.1773	2.9409	0.0041	−2.7082	2.0354	−0.0860	0.0072	0.0059
220	49H	Plate	0.1645	2.5393	0.0092	−100	0.0000	0.0000	−0.0213	−0.0264
220	49H	Rosette	0.1802	2.6557	0.0091	−4.6635	0.9596	−0.1577	−0.0008	−0.0020
220	49V	Column	0.1535	2.8991	0.0055	−1.7852	1.2741	−0.6830	0.0376	0.0342
220	49V	Hollow	0.1774	2.9262	0.0049	−1.9326	1.6027	−0.7670	0.0369	0.0346
220	49V	Plate	0.1630	2.5395	0.0123	−2.2822	1.5045	−0.6042	0.0760	0.0744
220	49V	Rosette	0.1780	2.6321	0.0130	−1.9668	1.2509	−0.8404	0.0366	0.0320
340	0	Column	0.1078	2.8760	0.0058	−1.2290	1.4847	−1.3773	0.1406	0.1707
304	0	Hollow	0.1247	2.8819	0.0055	−1.2102	1.2847	−1.4779	0.1342	0.1615
340	0	Plate	0.1094	2.5369	0.0093	−100	0.0000	0.0000	0.1948	0.2492
340	0	Rosette	0.1226	2.6283	0.0075	−3.1509	1.1632	−0.2190	0.0895	0.1148
340	49H	Column	0.1081	2.8524	0.0069	−1.8631	1.9070	−1.0067	0.0067	0.0000
340	49H	Hollow	0.1249	2.8641	0.0063	−1.6979	1.5986	−1.4333	0.0041	−0.0022
340	49H	Plate	0.1104	2.4788	0.0107	−100	0.0000	0.0000	−0.0519	−0.0620
340	49H	Rosette	0.1234	2.5819	0.0090	−3.9251	1.0819	−0.0267	−0.0142	−0.0189
340	49V	Column	0.1081	2.8293	0.0081	−1.3835	0.8047	−0.4362	0.0562	0.0494
340	49V	Hollow	0.1250	2.8488	0.0070	−1.3908	0.8007	−0.8232	0.0577	0.0525
340	49V	Plate	0.1090	2.4830	0.0154	−1.7342	1.0314	−0.5159	0.0739	0.0655
340	49V	Rosette	0.1218	2.5613	0.0136	−1.5634	0.6545	−0.6238	0.0310	0.0219

creases dramatically with the radiometer frequency. As the scattering gets beyond the Rayleigh regime, the extinction becomes less sensitive to the characteristic particle size, D_m. Thus, for the cirrus particle distributions considered here, even higher frequencies would be quite useful for increased signal and lower error from uncertainties in particle size. The different crystal shapes will have a significant effect on the radiative transfer. The extinction–polarization ratio results show that it might be possible to detect particle shape by using the polarization signature, but this will also depend on the characteristic particle size. The higher frequencies and larger particle size distributions considered here, which would have the highest optical depths, all have high single scattering albedo. Thus, these more detectable distributions would be in the scattering regime, where the upwelling radiation does not depend on the temperature of the ice cloud.

The companion paper (Part II) uses these single-scattering results in a polarized radiative transfer model to compute upwelling brightness temperatures. These are analyzed to examine the issues of, and develop po-

tential methods for, remotely sensing cirrus IWP using passive microwave radiometry. Many of the properties identified here with the single-scattering results will be found to be germane for microwave remote sensing of cirrus.

Acknowledgments. We acknowledge Dr. J. Vivekanandan for providing the EBCM oblate spheroid scattering results for comparison with the DDA. Financial support for this research was provided in part by NASA Grant NAG-5-1592S and NSF Grant ATM-9100795.

REFERENCES

Alishouse, J. C., S. A. Snyder, J. Vongasthorn, and R. R. Ferraro, 1990: Determination of oceanic total precipitable water from the SSM/I. *IEEE Trans. Geosci. Remote Sens.*, **28,** 811–816.

Barber, P., and C. Yeh, 1975: Scattering of electromagnetic waves by arbitrary shaped dielectric bodies. *Appl. Opt.*, **14,** 2864–2872.

Draine, B. T., 1988: The discrete dipole approximation and its application to interstellar graphite grains. *Astrophys. J.*, **333,** 848–872.

——, and J. Goodman, 1993: Beyond Clausius–Mossotti: Wave propagation on a polarizable point lattice and the discrete dipole approximation. *Astrophys. J.*, **405,** 685–697.

——, and P. J. Flatau, 1994: Discrete-dipole approximation for scattering calculations. *J. Opt. Soc. Amer. A,* **11,** 1491–1499.

Dungey, C. E., and C. F. Bohren, 1993: Backscattering by nonspherical hydrometeors as calculated by the coupled-dipole method: An application in radar meteorology. *J. Atmos. Oceanic Technol.*, **10,** 526–532.

Evans, K. F., and J. Vivekanandan, 1990: Multiparameter radar and microwave radiative transfer modeling of nonspherical atmospheric ice particles. *IEEE Trans. Geosci. Remote Sens.*, **28,** 423–437.

——, and G. L. Stephens, 1993: Microwave remote sensing algorithms for cirrus clouds and precipitation. Dept. of Atmospheric Science Tech. Rep. 540, Colorado State University, Fort Collins, CO, 198 pp.

——, and ——, 1995: Microwave radiative transfer through clouds composed of realistically shaped ice crystals. Part II: Remote sensing of ice clouds. *J. Atmos. Sci.*, **52,** 2058–2072.

Flatau, P. J., K. A. Fuller, and D. W. Mackowski, 1993: Scattering by two spheres in contact: Comparisons between discrete-dipole approximation and modal analysis. *Appl. Opt.*, **32,** 3302–3305.

Gasiewski, A. J., 1992: Numerical sensitivity analysis of passive EHF and SMMW channels to tropospheric water vaper, clouds, and precipitation. *IEEE Trans. Geosci. Remote Sens.*, **30,** 859–870.

Goedecke, G. H., and S. G. O'Brien, 1988: Scattering by irregular inhomogeneous particles via the digitized Green's function algorithm. *Appl. Opt.*, **27,** 2431–2437.

Goodman, J. J., B. T. Draine, and P. Flatau, 1991: Application of Fast-Fourier-Transform techniques to the discrete-dipole approximation. *Opt. Lett.*, **16,** 1198–1200.

Greenwald, T. J., G. L. Stephens, and T. H. V. Haar, 1993: A physical retrieval of cloud liquid water over the global oceans using special sensor microwave/imager (SSM/I) observations. *J. Geophys. Res.*, **98,** 18 471–18 488.

Heymsfield, A., 1972: Ice crystal terminal velocities. *J. Atmos. Sci.*, **29,** 1348–1357.

——, K. M. Miller, and J. D. Spinhirne, 1990: The 27–28 October 1986 FIRE IFO cirrus case study: Cloud microstructure. *Mon. Wea. Rev.*, **118,** 2313–2328.

Hollinger, J. P., J. L. Peirce, and G. A. Poe, 1990: SSM/I instrument evaluation. *IEEE Trans. Geosci. Remote Sens.*, **28,** 781–790.

Kosarev, A. L., and I. P. Mazin, 1989: Empirical model of physical structure of the upper level clouds of the middle latitudes. *Radiation Properties of Cirrus Clouds,* Nauka, 29–52.

Kummerow, C., and L. Giglio, 1994: A passive microwave technique for estimating rainfall and vertical structure information from space. Part I: Algorithm description. *J. Appl. Meteor.*, **33,** 3–18.

Liu, G., and J. A. Curry, 1993: Determination of characteristic features of cloud liquid water from satellite measurements. *J. Geophys. Res.*, **98,** 5069–5092.

Matrosov, S. Y., B. W. Orr, R. A. Kropfil, and J. B. Snider, 1994: Retrieval of vertical profiles of cirrus cloud microphysical parameters from Doppler radar and infrared radiometer measurements. *J. Appl. Meteor.*, **33,** 617–626.

Muller, B. M., H. E. Fuelberg, and X. Xiang, 1994: Simulations of the effects of water vapor, cloud liquid water, and ice on AMSU moisture channel brightness temperatures. *J. Appl. Meteor.*, **33,** 1133–1154.

O'Brien, S. G., and G. H. Goedecke, 1988: Scattering of millimeter waves by snow crystals and equivalent homogeneous symmetric particles. *Appl. Opt.*, **27,** 2439–2444.

Ono, A., 1969: The shape and riming properties of ice crystals in natural clouds. *J. Atmos. Sci.*, **26,** 138–147.

Platt, C. M. R., N. L. Abshire, and G. T. McNice, 1978: Some microphysical properties of an ice cloud from lidar observation of horizontally oriented crystals. *J. Appl. Meteor.*, **17,** 1220–1224.

Purcell, E. M., and C. R. Pennypacker, 1973: Scattering and absorption of light by nonspherical dielectric grains. *Astrophys. J.*, **186,** 705–714.

Sarkar, T. K., E. Arvas, and S. M. Rao, 1985: Application of the fast Fourier transform and the conjugate gradient method for efficient solution of electromagnetic scattering from both electrically large and small conducting bodies. *Electromagnetics,* **5,** 99–122.

Simpson, J., R. F. Adler, and G. R. North, 1988: A proposed tropical rainfall measuring mission (TRMM) satellite. *Bull. Amer. Meteor. Soc.*, **69,** 278–295.

Singham, S. B., and C. F. Bohren, 1987: Light scattering by an arbitrary particle: A physical reformulation of the coupled dipole method. *Opt. Lett.*, **12,** 10–12.

Spencer, R. W., W. S. Olson, W. Rongzhang, D. W. Martin, J. A. Weinman, and D. A. Santek, 1983: Heavy thunderstorms observed over land by the Nimbus 7 scanning multichannel microwave radiometer. *J. Climate Appl. Meteor.*, **22,** 1041–1046.

——, H. M. Goodman, and R. E. Hood, 1989: Precipitation retrieval over land and ocean with the SSM/I: Identification and characteristics of the scattering signal. *J. Atmos. Oceanic Technol.*, **6,** 254–273.

Tjemkes, S. A., G. L. Stephens, and D. L. Jackson, 1991: Spaceborne observations of columnar water vapor: SSMI observations and algorithm. *J. Geophys. Res.*, **96,** 10 941–10 954.

Warren, S. G., 1984: Optical constants of ice from the ultraviolet to the microwave. *Appl. Opt.*, **23,** 1206–1225.

Weinman, J. A., 1988: The effects of cirrus clouds on 118-GHz brightness temperatures. *J. Geophys. Res.*, **93,** 11 059–11 062.

Wilheit, T. T., and A. T. C. Chang, 1991: Retrieval of monthly rainfall indices from microwave radiometric measurements using probability distribution functions. *J. Atmos. Oceanic Technol.*, **8,** 118–136.

——, R. Adler, S. Avery, E. C. Barrett, P. Bauer, W. Berg, A. Chang, J. Ferriday, N. Grody, S. Goodman, C. Kidd, D. Kniveton, C. Kummerow, A. Mugnai, W. Olson, G. Petty, A. Shibata, E. A. Smith, and R. W. Spencer, 1994: Algorithms for the retrieval of rainfall from passive microwave measurements. *Remote Sens. Rev.*, **11,** 163–194.

Wu, M.-L. C., 1987: Determination of cloud ice water content and geometrical thickness using microwave and infrared radiometric measurements. *J. Climate Appl. Meteor.*, **26,** 878–884.